

Supplemental Material:
ROSE: Multi-Level Super-Resolution-Oriented Semantic Embedding for 3D Microvasculature Segmentation from Low-Resolution Images

1. Spatial and Frequency LR Dataset Generation

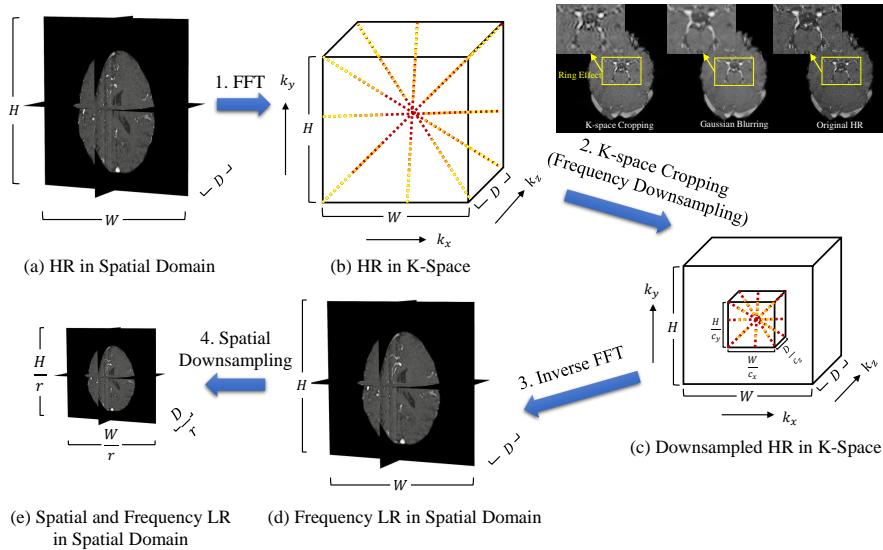


Figure 1: LR image generation flowchart. This process contains the downsamplings in both spatial and frequency domains, which better conforms with the real LR MRI image production. One can observe that small vessels are more dilated / blurred and the image contains strong ring-effect artifacts in the k-space downsampling compared with 3D Gaussian blurring, which implies that our task is more challenging than the traditional natural image downscaling.

In order to tackle the challenging 3D microvasculature segmentation and visualization scenario, we focus on SR microvasculature with complicated vessel geometry and topology as well as high sparseness in a noisy large-sized 3D volume. This SR microvasculature segmentation work covers the research

domains from MR data acquisition and image generation. The standard MRI scanners use a large static magnetic field to capture the MR signal and then obtain sampled sensor data in k-space (frequency space). This data acquisition requires specially designed MR sequences [1, 2, 3, 4]. Once the sampled sensor data are captured, 3D MRI images can be reconstructed from k-space.

Motivation. The image SR / LR process is essentially the process to increase the image resolution from low to high or vice versa. Unlike natural images, the proposed MRI image SR / LR task is more challenging due to the intrinsic physic acquisition mechanism. There is an essential formulation difference between these two kinds of images, which implies their SR / LR counterpart acquisition methods are different. Specifically, LR natural images are generated through downsampling (and / or along with some blurring filters) in the spatial domain; instead, the LR MRI image downsampling explicitly happens both in the spatial and frequency domains, i.e., k-space [5, 2].

Computations. In medical practice, the outcomes of this work can be used as the key functions for real-time generating *in-vivo* higher-resolution 3D semantic microvascular structures with better quality by using faster (lower-resolution) scanning. In this subsection, we will discuss how to use the current HR MRI images (as image ground truth) to generate their LR counterpart as network inputs under domain experts' guidance. The ground truth vessel labels are generated on HR images and more details are given in Section 4.1 of the main paper. Suppose we have an HR MRI image I with spatial size $W \times H \times D$, the detailed downsampling processes in both spatial and frequency domains to obtain the corresponding LR image I' are as follows. Figure 1 shows the overall LR image generation flowchart.

1. Apply fast Fourier transform (FFT) on I to convert it into k-space and then apply FFT shift to align the k-space center to the 3D space center;
2. Determine the k-space downsampling factors c_x , c_y , and c_z along two MR phase encoding axes k_x , k_y and the slicing encoding axis k_z . Crop a box of size $\frac{W}{c_x} \times \frac{H}{c_y} \times \frac{D}{c_z}$ at k-space center and zero pad the values beyond the box. This process removes the detailed / high frequencies at the outer space and only keeps the contrast frequencies at the center, which resembles the LR MRI image acquisition essentially;
3. Apply FFT shift and inverse FFT to convert the k-space data back to its spatial domain to obtain I' . The grayscale range of I is usually

- sightly higher than I' due to higher level of noise;
4. Determine the spatial downsampling factor r and shrink the size of I' to $\frac{W}{r} \times \frac{H}{r} \times \frac{D}{r}$ in spatial domain.

The above downsampling process explicitly happens both in the spatial and frequency domains, which mimics the real formulation / acquisition of an LR MRI image more accurately. In addition, it is noted that the LR image downsampled in k-space has quite different blurring patterns compared with that from the alternative spatial image downsampling techniques. The spatial and frequency LR image generates more dilated / blurred small structures and contains the additional artifacts, e.g., the ring effect as indicated in zoomed-in areas in Figure 1, which do not exist in the simple Gaussian blurring LR image (or any other spatial smoothing filters). In this case, it makes our task even more challenging for fine / micro vessel segmentation and SR computation than the corresponding task on the traditional natural image.

2. Supplemental Experiments

2.1. Additional Results

This section demonstrates additional qualitative results and illustrations, such as 3D visualization of two testing results on MICRO-MRI SWI dataset by our ROSE method in Figure 2, additional 3D surface rendering comparison between our method and state-of-the-art SR-based segmentation, i.e., DSRL [6], SegSRGAN [7], PFSeg [8], and vessel segmentation, i.e., (Pre-Int.) ATRG [9], (Pre-Int.) LiviaNET [10], (Pre-Int.) DVN [11], (Pre-Int.) Full 3D U-Net [12], on brain subareas of $S_{29} - S_{42}$, including very dense microvasculature distribution, from one testing case of MICRO-MRI dataset in Figure 3, additional image-based visualization comparison between our method and state-of-the-art SR-based segmentation methods (i.e., DSRL [6], SegSRGAN [7]) on MICRO-MRI dataset from an image slice in Figure 4, additional image-based visualization comparison between our method and state-of-the-art vessel segmentation methods on MICRO-MRI dataset from an image slice in Figure 5, original HR and downsampled LR image (for inputs) examples from TubeTK MRA and MICRO-MRI datasets in our ROSE method in Figure 6.

2.2. Additional Results on Abnormal Micro Vessel Segmentation

Figure 7 shows some additional qualitative results on abnormal micro vessel extraction and visualization. The HR SWI data were collected on a patient with relapsing-remitting multiple sclerosis (RRMS) on a 3T MRI scanner. The anomaly caused by RRMS can be traced by the appearance of the box-like developmental venous anomaly (DVA) as shown in Figure 7. DVAs contain a group of veins, formed in an irregular pattern, and are generally situated closer to each other than normal (causing high vascular density in that region). Specifically, the typical box-like DVA pattern mainly locates in the second and the third slices while the first slice shows how the box-like DVA drains in to the connecting larger vessel. Our method does better in capturing this abnormal pattern compared to 3D U-Net [12] (with Pre-Int.), especially in the second slice, which is very crucial in clinical studies for precision diagnosis of microvascular disease.

References

- [1] G. Wright, Magnetic resonance imaging, *IEEE Signal Processing Magazine* 14 (1) (1997) 56–66.
- [2] Z.-P. Liang, P. Lauterbur, P. Lauterbur, Principles of magnetic resonance imaging (2000).
- [3] S. Huettel, A. Song, G. McCarthy, et al., Functional magnetic resonance imaging, Vol. 1, Sinauer Associates Sunderland, MA, 2004.
- [4] R. Brown, Y.-C. Cheng, E. Haacke, M. Thompson, R. Venkatesan, Magnetic resonance imaging: physical principles and sequence design, John Wiley & Sons, 2014.
- [5] R. Mezrich, A perspective on k-space, *Radiology* 195 (2) (1995) 297–316.
- [6] L. Wang, D. Li, Y. Zhu, L. Tian, Y. Shan, Dual super-resolution learning for semantic segmentation, in: Proceedings of the IEEE/CVF Conference on Computer Vision and Pattern Recognition, 2020, pp. 3774–3783.
- [7] Q. Delannoy, C.-H. Pham, C. Cazorla, C. Tor-Díez, G. Dollé, H. Meunier, N. Bednarek, R. Fablet, N. Passat, F. Rousseau, SegSR-GAN: Super-resolution and segmentation using generative adversarial

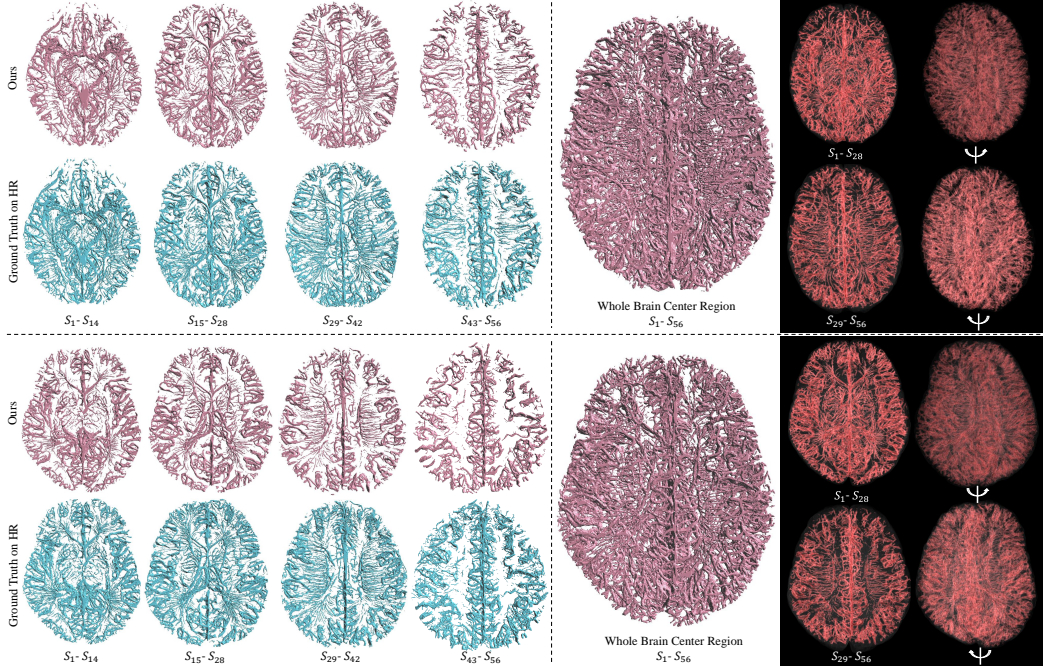


Figure 2: Different qualitative 3D segmentation visualizations of two testing results on MICRO-MRI SWI dataset from superior direction. Left: Comparison of different non-overlapping brain subareas between the results from our ROSE and the ground truth by surface rendering. Middle: Overview of the super dense whole region from center of the brain microvasculature prediction results from ROSE by surface rendering. Right: Volume rendering of these two testing cases from ROSE, first viewing from superior direction and displayed as halves, and then viewing from slightly rotated angles ($\sim 30^\circ$) along sagittal axis (upper: counterclockwise, lower: clockwise) as whole brain center regions.

networks-application to neonatal brain MRI, Computers in Biology and Medicine 120 (2020) 103755.

- [8] H. Wang, L. Lin, H. Hu, Q. Chen, Y. Li, Y. Iwamoto, X.-H. Han, Y.-W. Chen, R. Tong, Patch-free 3D medical image segmentation driven by super-resolution technique and self-supervised guidance, in: Proceedings of the Medical Image Computing and Computer Assisted Intervention, 2021, pp. 131–141.
- [9] J. Jiang, M. Dong, E. Haacke, ARGDYP: an adaptive region growing and dynamic programming algorithm for stenosis detection in MRI, in:

Proceedings of IEEE International Conference on Acoustics, Speech, and Signal Processing, Vol. 2, 2005, pp. ii–465.

- [10] J. Dolz, C. Desrosiers, I. B. Ayed, 3D fully convolutional networks for subcortical segmentation in MRI: A large-scale study, NeuroImage 170 (2018) 456–470.
- [11] G. Tetteh, V. Efremov, N. Forkert, M. Schneider, J. Kirschke, B. Weber, C. Zimmer, M. Piraud, B. Menze, DeepVesselNet: Vessel segmentation, centerline prediction, and bifurcation detection in 3-D angiographic volumes, arXiv preprint arXiv:1803.09340 (2018).
- [12] Ö. Çiçek, A. Abdulkadir, S. Lienkamp, T. Brox, O. Ronneberger, 3D U-Net: learning dense volumetric segmentation from sparse annotation, in: Proceedings of International Conference on Medical Image Computing and Computer Assisted Intervention, 2016, pp. 424–432.

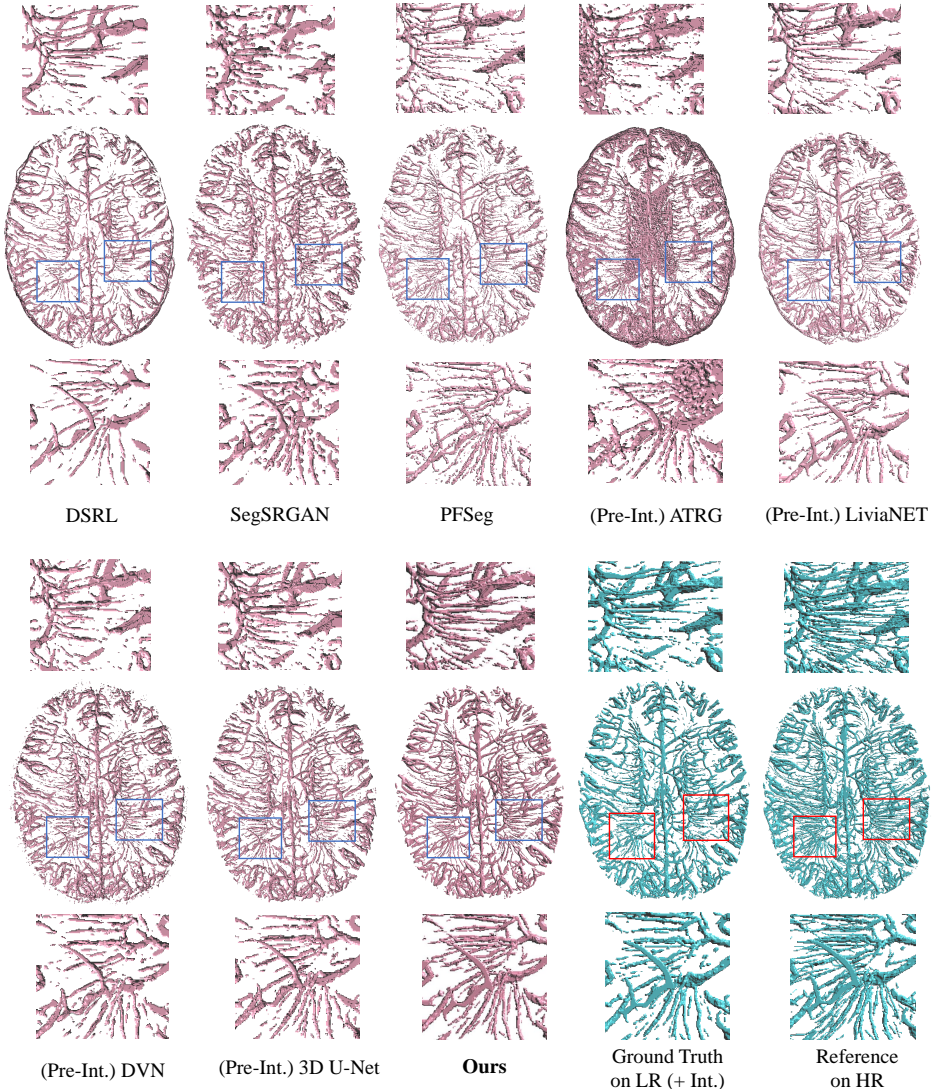


Figure 3: Additional qualitative 3D surface rendering visualization comparison between our method and state-of-the-art SR-based segmentation and vessel segmentation on brain subareas of $S_{29} - S_{42}$, including very dense microvasculature distribution, from one testing case of MICRO-MRI dataset. It is noted that the input of all these methods is LR image and the output is the segmentation based on LR image input. Here we also show the ground truth of vessel label (with interpolation) on LR image for the comparison. Our method exceeds the quality of the ground truth with interpolation on LR images, and is even close to the quality of the reference produced directly on HR images.

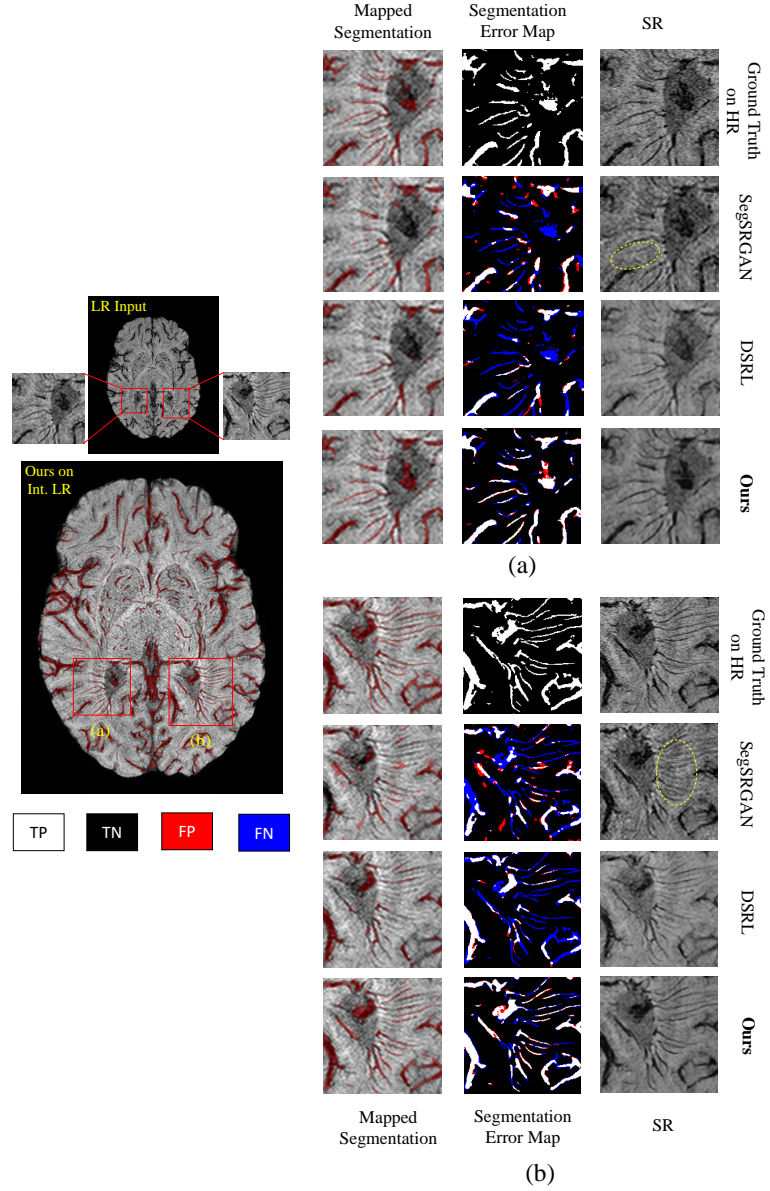


Figure 4: Additional qualitative comparison between our method and state-of-the-art SR-based segmentation methods on MICR-MRI dataset. Two patches (a) and (b) from a single slice are zoomed in for the evaluation. In each patch, we visualize the SR results, segmentation error maps, and the semi-transparent red vessel masks mapped on the interpolated LR SWI image (as a background) from our customized GUI tool. In the error maps, we use white color for True Positive (TP), black color for True Negative (TN), red color for False Positive (FP), blue color for False Negative(FN).

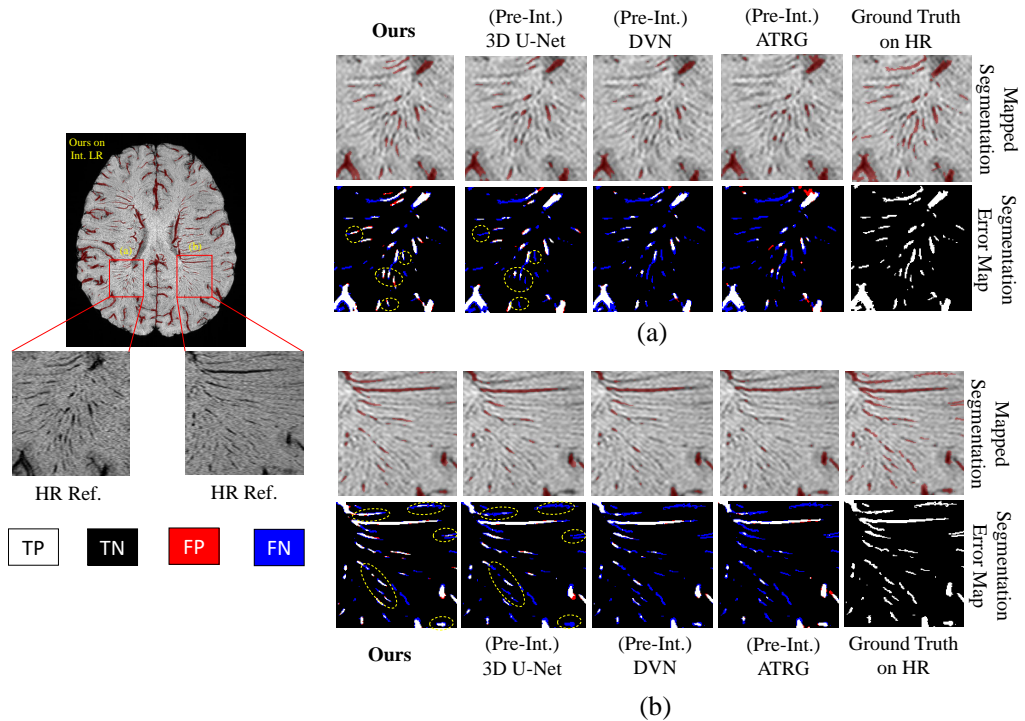


Figure 5: Additional qualitative comparison between our method and state-of-the-art vessel segmentation methods on MICRO-MRI dataset. Two patches (a) and (b) are selected from two typical brain regions on a single slice, where micro-level vessels are intensively distributed. Some subtle differences are circled in yellow. Segmentation error maps, vessel masks mapped on the interpolated LR SWI image, and the HR SWI patch reference are provided.

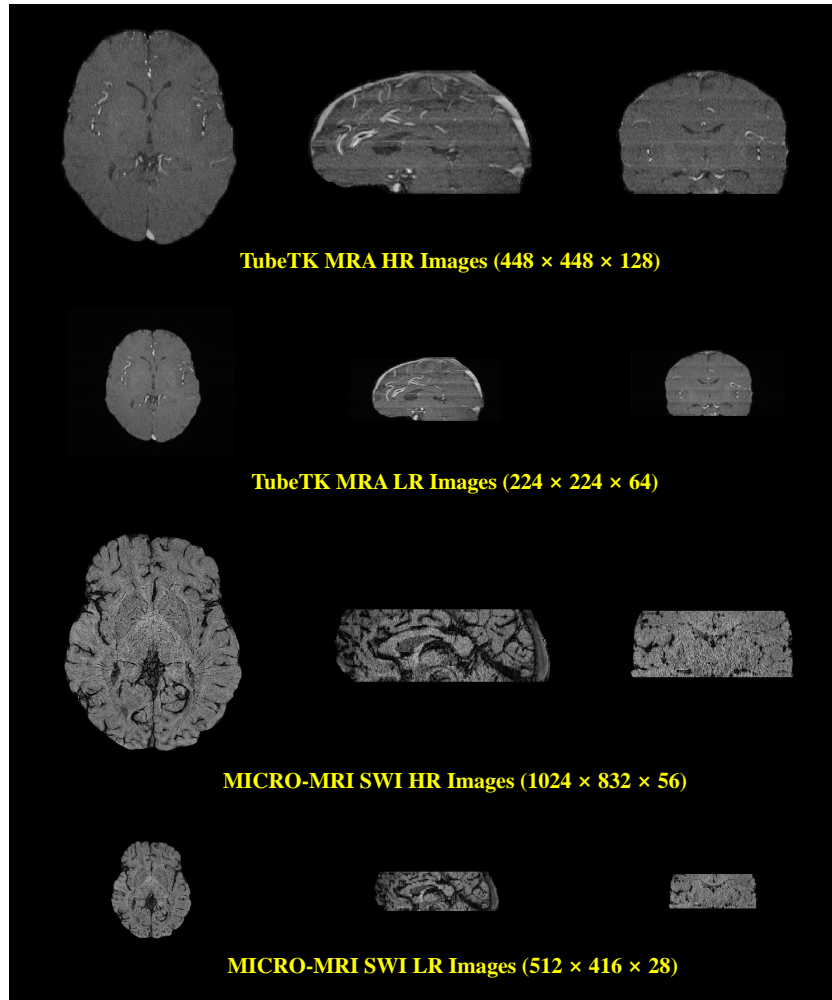


Figure 6: Original HR and downsampled LR image (for inputs) examples from TubeTK MRA and MICRO-MRI datasets in our ROSE method.

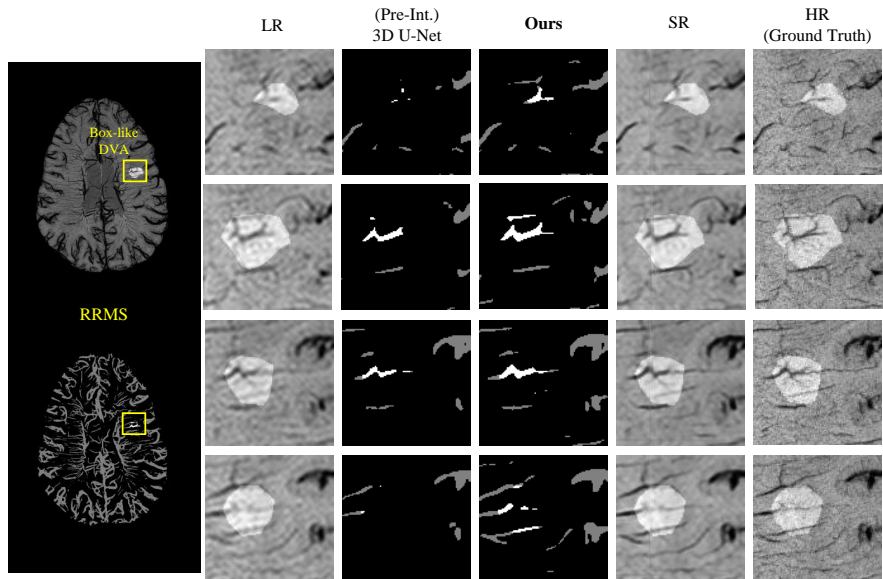


Figure 7: Additional visualization comparison on one vascular anomaly case (RRMS) between 3D U-Net (with Pre-Int.) and our method. The leftmost column show HR SWI image mIP (Minimum Intensity Projection) along with our predicted vessel mask MIP (Maximum Intensity Projection) with regions of interest (ROIs) highlighted. The zoomed-in patches (with different volume slices) in different formats are listed for detail examination. (Note that the LR input SWI images are interpolated to the same size of the HR ones for a better examination, and the actual input size is halved along three axes).